Direct numerical simulation on the effects of surface slope and skewness on rough-wall turbulence

Direct numerical simulation on the effects of surface slope and skewness on rough-wall turbulence

Y. Kuwata (桑田 祐丞)[1] and R. Nagura (名倉 梨花)[1]
Department of Mechanical Engineering, Osaka Prefecture University, 1-1 Sakai, Osaka, 599-8531, Japan [a)]

(Dated: 3 December 2020)

This paper presents direct numerical simulation (DNS) results of turbulent flows over systematically varied rough surfaces. Three-dimensional irregular rough surfaces with varying effective slope and skewness factor and fixed roughness height scales were considered in the study. The skewness factor characterizes whether the surface of interest has a peak-dominated or valley-dominated nature, whereas the effective slope measures the wavelength of the surface undulations or solidity of the roughness elements. The influence of these two topological parameters on the friction drag at rough surfaces was investigated. Downward shifts in the inner-scaled mean velocity, which quantify an increase in the friction drag, were found to be larger for surfaces with a positive skewness factor, and this trend was found to be more pronounced as the effective slope increased. In addition, the downward shift value steeply increased with increases in the effective slope, while the dependence weakened when the effective slope was larger than a certain threshold value. The physical mechanism behind the increase in the roughness function was investigated by analyzing the momentum budgets. It was revealed that the viscous drag dominantly contributes to the roughness function when the effective slope value is small, whereas the contribution by the pressure drag progressively increases with the effective slope. We also found that for surfaces with larger effective slope consisting of relatively shorter wavelength undulations, the Reynolds shear stress tends to be reduced because the wall roughness prevents the formation of quasi-streamwise elongated vortices suppressing the turbulent near-wall cycles. This acts as a negative contribution to the roughness function, and the two competing effects (of the increase in pressure drag and decrease in Reynolds shear stress) weaken the dependence of the effective slope value on the roughness function. Further analysis was conducted to better understand how the surface slope and skewness factor values affect the mean flow field, modifying the pressure and viscous drag forces.

I. INTRODUCTION

Rough-wall turbulence has received significant attention over the past decades because surfaces in engineering systems are seldom hydraulically smooth but typically have roughness. The surface of a turbine blade becomes rough over time owing to deposition, pitting, and spallation that occur while operating in harsh conditions. Similarly, time-related deterioration, including erosion, corrosion, and organic and inorganic fouling processes, generate roughness in ship hulls, oil pipelines, and heat exchangers. In most situations, the flow in these systems is turbulent, and the wall roughness is not within the viscous sublayer but protrudes into the logarithmic layer, leading to a significant increase in friction drag. Consequently, this results in substantial performance degradation of the aforementioned systems. Hence, predicting turbulence modification due to wall roughness becomes an important prerequisite for optimal engineering design and machine maintenance. To quantify such surface roughness effects, the equivalent roughness k_s and the roughness function ΔU^+ have been widely employed. The equivalent roughness is defined as the size of sand grain that yields the same skin friction coefficient as the surface of interest, and ΔU^+ is the downward shift value in the inner-scaled mean velocity profile in the logarithmic region.

One of the important characteristic that has a significant impact on surface roughness effects is the solidity of the roughness elements. Earlier works on the influence of solidity for two-dimensional surface roughness were conducted by Bettermann[1], Dvorak[2], and Dirling[3]. Dirling[3] provided correlations for k_s based on two parameters: a solidity parameter and a shape parameter. The solidity parameter was represented as the ratio of the average element spacing to roughness height, while the shape parameter accounted for the frontal area and the windward wetted surface area of a single roughness element. An alternative expression including the solidity parameter Λ was proposed by Sigal and Danberg[4], which was based on the reference surface area before the addition of roughness and the total frontal area over the rough surface. Another representation for solidity, which is significantly easier to define for three-dimensional irregular roughness, is the effective slope (ES) proposed by Napoli *et al.*[5]; it is defined as follows:

$$ES = \frac{1}{L_x L_z}\int_x\int_z \left|\frac{\partial h(x,z)}{\partial x}\right| dxdz, \qquad (1)$$

where $h(x,z)$ is the roughness height, and L_x and L_z are the respective streamwise and spanwise lengths of the rough surface. ES is defined as the average value of the magnitude of the slope of the roughness corrugation, and it can be shown that ES is double the value of the solidity parameter: $ES = 2\Lambda$[5–7]. To demonstrate the ability of ES in predicting surface roughness effects, Napoli *et al.*[5] performed a large eddy simulation (LES) of two-dimensional irregular corrugated walls and found that the roughness function ΔU^+ increased with the ES value when the ES value was lower than a certain threshold. They also showed that flow separation behind the roughness crest occurred more frequently as the ES value increased, and this increased the contribution of the pressure drag to the total friction drag. A simi-

[a)]Electronic mail: kuwata@me.osakafu-u.ac.jp

lar trend of dependence of the ES value on ΔU^+ was confirmed via experiments on closely packed pyramids[8] and direct numerical simulation (DNS) studies on sinusoidal wavy walls[9], randomly distributed semi-ellipsoid/cone roughness[10], and a variety of real rough surfaces such as concrete, grit-blasted, and graphite[6]. Using large amounts of LES data, De Marchis[11] proposed a new mathematical logarithmic law that could reasonably predict ΔU^+ based on the ES value. Yuan and Jouybari[12] provided a physical interpretation of a relatively smaller drag for a surface with a small ES value. They stated that the occurrence of roughness wakes was decreased for the surface with the small ES value, thus reducing the pressure drag. In addition, they reported that the energy redistribution to the wall-normal Reynolds stress was attenuated for the surface with small ES value, owing to the reduction in the form-induced shear and mixing-layer turbulence activity. Extensive investigations on the effects of solidity were also conducted by MacDonald *et al.*[7] as well as Leonardi and Castro[13], who also focused on surfaces with densely distributed roughness elements. MacDonald *et al.*[7] showed that although ΔU^+ first increased with the ES value as reported in Napoli *et al.*[5], it decreased in the dense roughness regime with larger ES values. They stated that this trend was consistent with the observations in the so-called $d-$type roughness[14], and the driving mechanism was attributed to a reduction in the Reynolds shear stress that was predominantly due to the near-wall turbulence cycle being pushed away from the rough wall.

The other important characteristic parameter for determining surface roughness effects is the skewness factor (Sk). The skewness factor, which is defined by the statistical moments of the surface elevation, quantifies the asymmetry of the probability density function (PDF) of the roughness height elevation. The skewness factor Sk is defined as follows:

$$Sk = \frac{1}{h_{rms}^3 L_x L_z} \int_x \int_z (h(x,z) - h_m)^3 \, dxdz, \quad (2)$$

where h_m is the mean roughness height, and h_{rms} is the root-mean-square roughness height:

$$h_{rms}^2 = \frac{1}{L_x L_z} \int_x \int_z (h(x,z) - h_m)^2 \, dxdz. \quad (3)$$

The skewness factor characterizes whether the surface of interest has a peak-dominated or valley-dominated nature: a surface with a positive Sk value is peak-dominated whereas a surface with a negative value is valley-dominated. An earlier attempt to relate the statistical moments of the surface elevation to the equivalent roughness was made by Musker[15], and many correlations toward predicting the surface roughness effects using the skewness factor have been proposed[6,10,16–18]. A large amount of experimental data for several types of rough surfaces, including packed spheres, sandpaper, gravel, honed pipes, and scratched plates, suggested that the surface roughness effects were enhanced with an increasing Sk value when $Sk > -1$[16]. This has also been corroborated by recent DNS studies[6,10,18–20]. Measurements of a systematically varied surface by Flack *et al.*[21] revealed that a dramatic increase in friction drag occurred when the Sk value changed from a negative value to zero, while a change from zero to a positive value caused a modest increase in friction drag. A similar experimental study by Flack *et al.*[22] suggested the need for separate predictive equations for surfaces with positive and negative skewness values. However, Flack *et al.*[22] as well as Busse *et al.*[20] reported that the transitional behavior toward the fully rough regime was almost independent of the Sk value. Jelly and Busse[23] discussed surface roughness effects using DNS for three roughness topographies: a Gaussian surface, a peaks-only surface, and a pits-only surface characterized by zero, positive, and negative Sk values, respectively. They reported that the peaks-only surface with a positive Sk value yielded a ΔU^+ comparable to that of the Gaussian surface, while the ΔU^+ for the pits-only surface with a negative Sk value was much smaller. The significantly larger ΔU^+ value for the peaks-only surface in comparison with that for the pits-only surface was mainly attributed to the velocity offset at the roughness crest, which represented the integral effects of pressure and the viscous effects below the roughness crest.

As mentioned above, systematic investigations on Sk or ES have been carried out experimentally[8,22,24] and numerically[6,7,10,18,23,25], and the importance of Sk and ES values for determining surface roughness effects has been well established. Meanwhile, it has also been reported that many other important characteristic parameters need to be taken into account when predicting surface roughness effects (e.g., the Kurtosis defined as the fourth-order statistical moment[10,15], diversity of roughness peak heights[10,26], and streamwise correlation length[6], as well as roughness height scales such as mean peak height, peak-to-valley height, and roughness height amplitude). This causes difficulties in isolating the influence of each characteristic parameter on surface roughness effects, and remains a major obstacle in appropriately accounting for these characteristic parameters predicting the effects of surface roughness.

To resolve these difficulties, we investigated the individual effects of skewness Sk and slope (solidity) ES on surface roughness effects through DNSs of turbulence over three-dimensional irregular rough surfaces, in which the Sk and ES values were systematically varied while the other characteristic parameters remained fixed. Further, to better understand how these parameters (Sk and ES) affect the flow structure and momentum transport mechanisms, this study also analyzed the double-averaged (spatial and Reynolds) momentum equation.

II. FLOW CONDITIONS

As in the previous DNS studies[10,13,18,27,28], we chose a rough-walled open channel flow configuration as shown in Fig. 1 in which a flow is periodic in the streamwise and spanwise directions whereas the slip boundary conditions are applied at the top wall. Although the flow near the slip wall is not identical to that near the symmetry plane in full channel flow, the choice of the so-called open channel flow allows us to simulate turbulence modification near the rough wall with fewer computational resources. The computational domain size (L_x, L_y, L_z) is $(6\delta, \delta, 3\delta)$ in the streamwise, wall-normal, and spanwise directions, respectively, where δ is the half-channel height. The flow is driven by a constant streamwise pressure difference, and the friction Reynolds number based on the effective half-channel height, $\delta_e = \delta - h_m$ with h_m being the mean rough surface height, is fixed at $\mathrm{Re}_\tau = 600$. Here, the friction velocity u_τ is given by the averaged wall-shear stress $u_\tau = \sqrt{\tau_w/\rho}$, which is computed by the streamwise momentum balance between the pressure drop ΔP and the wall-shear stress:

$$\Delta P S_{yz} = \tau_w L_x L_z, \tag{4}$$

where $S_{yz} = V_f/L_x$ is the averaged fluid phase $y-z$ plane area with V_f being the volume of the fluid phase and can be simply written as $S_{yz} = \delta_e L_z$ (Kuwata and Kawaguchi[18]). Hence, we can obtain the wall-shear stress as follows:

$$\tau_w = \delta_e \frac{\Delta P}{L_x}. \tag{5}$$

It should be noted that the τ_w given by Eq.(5) is equivalent to the $x-z$ plane-averaged total shear stress extrapolated at the location of the mean roughness height. This definition is consistent with those employed in previous DNS studies[9,10,18,29]. In this study, we considered the lattice Boltzmann equation for the governing equation, which is proven to recover the continuity and Navier–Stokes equations in second-order accuracy in space and time. Although there are several possible choices for the LBM models, we used the three-dimensional twenty-seven (D3Q27) discrete velocity multiple-relaxation-time lattice Boltzmann method (LBM)[30]. This DNS approach has been validated against turbulent channel flows, and no perceptible differences were found between the mean velocity, second moments, energy spectra, and turbulent budget terms of the solutions from the LBM and spectral methods[30]. Further, the present LBM-DNS approach was successfully applied in turbulent flows over complicated rough surfaces[18,28,31,32]. The LBM employs a regular grid with equal spacing in which non-body-fitted Cartesian mesh to describe the rough-wall geometry. This feature reduces numerical errors arising from a coordinate transformation procedure; however, it requires prohibitively high computing resources for handling the entire computational domain with sufficiently fine grid resolution. Hence, the local grid refinement technique proposed by Kuwata and Suga[33] was adopted to allocate the doubly refined grid near the rough-wall region for $0 < y < 0.34\delta$. The grid resolution near the rough-wall region was determined such that the grid spacing in wall units is less than 2.0, as in the previous lattice Boltzmann DNS studies[18,28,29,32]where the wall unit is defined as u_τ/ν with ν denoting the kinematic viscosity. As a result, the total number of grid points was approximately 293 million. To handle the rough wall geometry, we employed the linear interpolated bounce-back method, as in the previous DNS studies[18,28,29,32]. This method is based on the bounce-back rule and accurately imposes no-slip boundary conditions to the rough surface with second-order accuracy[34]. The numerical setup, including the domain size and grid resolution, is comparable to those employed in previous DNS studies on rough-walled open channel flows[18,28,31,35]; therefore, it has been confirmed to be sufficient for capturing the full spectrum of scales, ranging from dissipative fine eddies to large-scale fluctuations.

TABLE I. Characteristic parameters of rough surfaces; *Sk* is the skewness factor, *ES* is the effective slope, h_{rms} is the root-mean-square roughness, h_a is the surface height amplitude, and h_t is the mean peak-to-valley height.

Sk	*ES*	h^+_{rms}	h^+_a	h^+_t	h_{rms}/δ_e
±0.53	0.1, 0.2, 0.4, 0.6	8.4	6.7	49	0.014

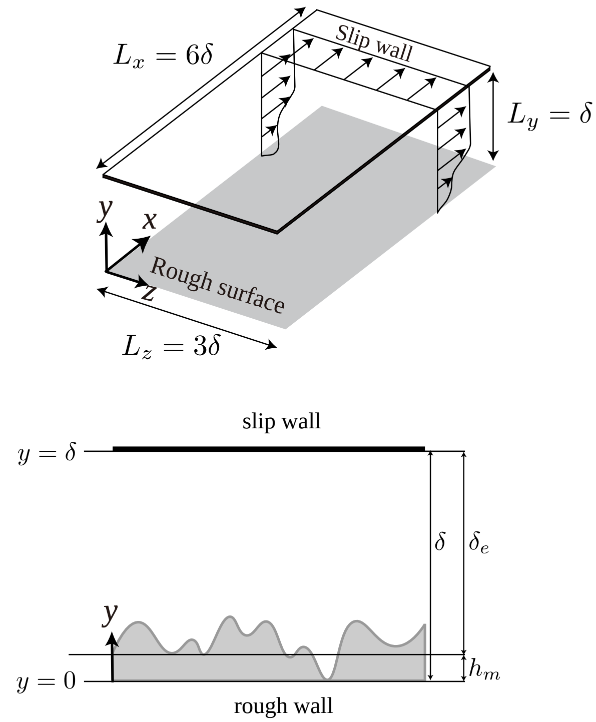

FIG. 1. Schematic of flow geometry of a rough-walled open channel flow.

III. ROUGH SURFACES

In this study, we considered 8 rough surfaces in which the *Sk* and *ES* values were systematically varied while the roughness height scales remained fixed. As mentioned previously, the skewness factor *Sk*, defined in Eq. (2), measures whether the surface of interest has a valley-dominated or a peak-dominated nature, whereas the effective slope *ES*, defined in Eq. (1), measures the wavelength of the surface undulations or solidity of the roughness elements. In what follows, we describe the procedure used for generating the rough surfaces. The surface height $h(x,z)$ was first generated by superimposing differently sized hyperbolic shape roughness elements. The height of a single hyperbolic shape roughness element $h_N(x,z)$ is defined as a rotating body of the hyperbolic

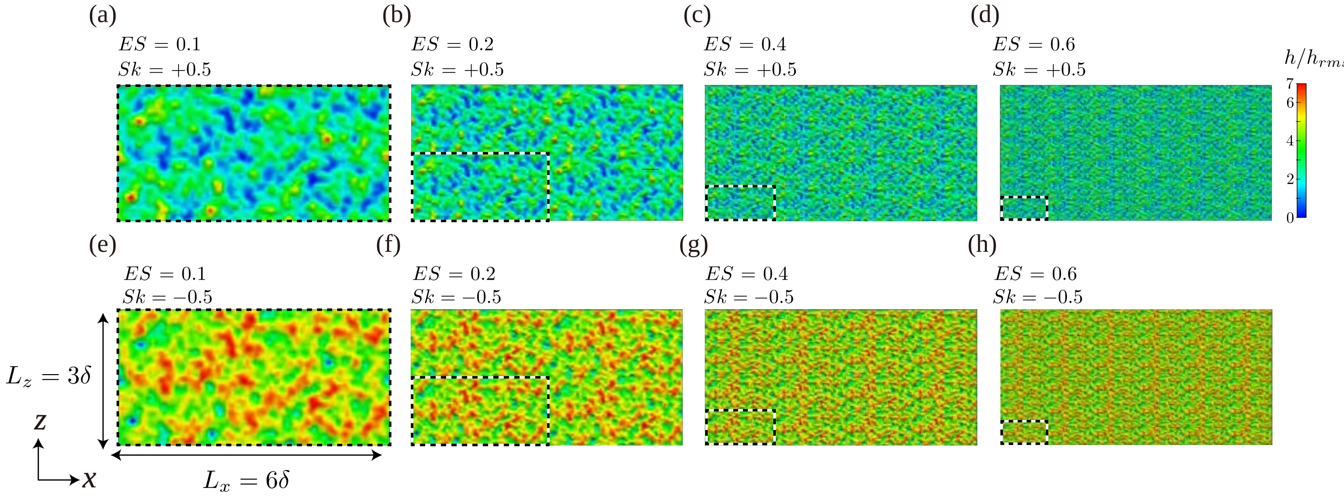

FIG. 2. Geometry of the rough surfaces together with the effective slope value in Eq. (1) and the skewness factor in Eq. (2). The surface enclosed by a dashed line indicates a single unit tile. 2×2, 4×4, 6×6 tiles are used for (b,f), (c,g), and (d,h), respectively.

function:

$$h_N(x,z) = (A_N \delta)\text{sech}\left(B_N \frac{\sqrt{(x-x_N)^2 + (z-z_N)^2}}{\delta}\right), \quad (6)$$

where x_N and z_N represent the center position of the roughness element, and the shape parameters A_N and B_N determine the height and width of a roughness element, respectively. Then, the rough surface height is given by superimposing the roughness elements as follows:

$$h(x,z) = \sum_N h_N(x,z), \quad (7)$$

where N denotes the number of roughness elements, and x_N, z_N, A_N, and B_N are all given by random numbers. The surface characteristics can be controlled through the number of roughness elements N and by imposing the upper and lower limits for the A_N and B_N values. The values for N, A_N, and B_N were adjusted by trial and error such that the Sk and ES values were close to the target values of $Sk = +0.53$ and $ES = 0.1$. The resulting values for these parameters are $N = 10000$, $1.2 \times 10^{-3} \leq A_N \leq 1.2 \times 10^{-2}$, and $14.4 \leq B_N \leq 28.8$, and the generated rough surface is shown in Fig. 2(a) including the Sk and ES values. Next, we describe how the ES and Sk values were systematically changed. The sign of the Sk value was changed by reversing the surface height as $h_p - h(x,z)$ with h_p being the maximum roughness peak. This transformed the surface peaks of the original rough surface into surface valleys in the reversed surface; this is clearly shown in Fig. 2(a,e), where the positions of the surface peaks in Fig. 2(a) correspond to the positions of the surface valleys in Fig. 2(e). Notably, this transformation did not affect the surface height scales and the ES value. The ES value was increased by reducing the surface width in the streamwise and spanwise directions while preserving the surface height. This procedure effectively altered the wavelength of the surface undulation but kept the roughness height scales fixed. For example, as shown in Fig. 2 (a,b), we reduced the width of the original surface (Fig. 2 (a)) in the streamwise and spanwise directions by a factor of 2; and when 2×2 reduced surfaces are used, the ES value is doubled, as shown in Fig. 2 (b). Following this procedure, the ES value was increased from 0.1 to 0.6; this range of ES values covers wavy surface to rough surface regimes[8]. The characteristic parameters, including the values of Sk, ES, and h_{rms}; the surface height amplitude h_a; and the mean peak-to-valley height h_t, are summarized in Table I, where h_t is computed by partitioning the surface in Fig. 2(a) into 5×5 tiles of equal size[6]. It should be noted that unlike other systematic studies on the characteristic parameters of a rough surface, this procedure only modified the ES and SK values and strictly preserved the roughness height scales (e.g., root-mean-square roughness, mean peak-to-valley height, and surface height amplitude) and the kurtosis; this allows us to investigate the isolated effects of ES and Sk values on turbulence. However, on the negative side, this procedure reluctantly imposes the repetition of the surface height in x and z directions for cases with $ES = 0.2, 0.4$, and 0.6. Thus, these surfaces cannot be regarded as perfectly irregular rough surfaces, and the effects of the roughness arrangement may appear; these aspects are discussed in §V. Note that, as shown in Fig.3, the grid resolution is sufficiently fine to accurately reproduce the surface geometry, even for the case with $ES = 0.6$, which has the steepest surface undulations among the presently tested cases.

IV. AVERAGING PROCEDURE

To statistically discuss turbulence near the rough wall, where a time-averaged variable changes in the $x-z$ plane due to the inhomogeneous nature of the surface, we focus on a variable averaged over space and time in the following discussion. For spatial averaging, we introduce superficial $x-z$

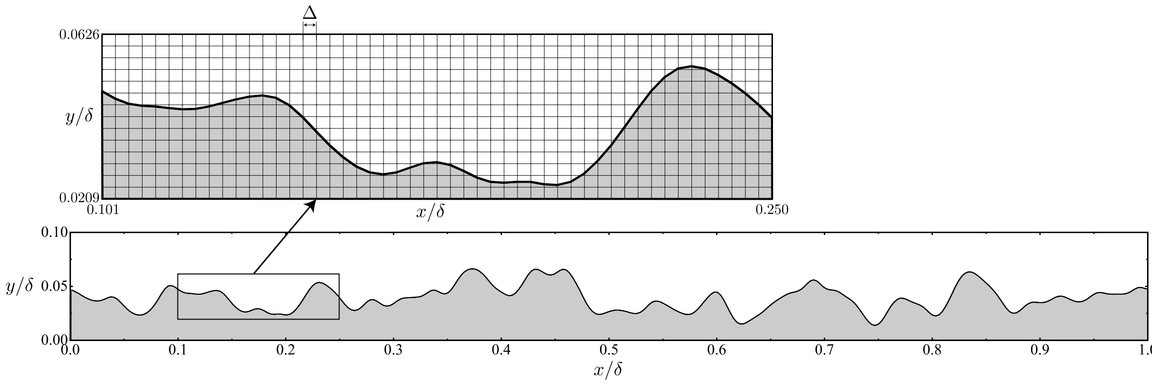

FIG. 3. Grid resolution near the rough surface for case with $ES = 0.6$ and $Sk = +0.53$. Here, Δ denotes the near-wall grid spacing.

plane-averaging for a variable $\phi(x,y,z)$ as follows:

$$\langle\phi\rangle(y,t) = \frac{1}{S}\int_x\int_z \phi(x,y,z,t)dxdz, \tag{8}$$

where the plane area $S = L_xL_z$. We can also define the variable averaged over a fluid phase $x-z$ plane as the intrinsic (fluid phase) averaged value:

$$\langle\phi\rangle^f(y,t) = \frac{1}{S_f}\int_x\int_z \phi(x,y,z,t)dxdz, \tag{9}$$

where S_f is the fluid phase $x-z$ plane area, and a relation exists between the superficial and intrinsic plane-averaged values as: $\langle\phi\rangle = \varphi\langle\phi\rangle^f$, with the plane porosity $\varphi = S_f/S$. The variable $\phi(x,y,z,t)$ can be decomposed into a contribution from an intrinsic averaged value $\langle\phi\rangle^f(y,t)$ and a deviation from the intrinsic averaged value $\tilde{\phi}(x,y,z,t)$ referred to as the dispersion, as follows:

$$\phi(x,y,z,t) = \langle\phi\rangle^f(y,t) + \tilde{\phi}(x,y,z,t). \tag{10}$$

As the flow variables also fluctuate in time, the Reynolds decomposition is introduced to decompose a variable into a Reynolds (ensemble) averaged value $\overline{\phi}(x,y,z)$ and its fluctuation $\phi'(x,y,z,t)$ as

$$\phi(x,y,z,t) = \overline{\phi}(x,y,z) + \phi'(x,y,z,t), \tag{11}$$

For Reynolds averaging, the statistical properties were assembled over a period of $250T$, where $T = L_x/U_b$ is the flow-through time and U_b is the bulk mean velocity.

V. MEAN VELOCITY AND ROUGHNESS FUNCTION

We first present profiles of the streamwise mean velocity to discuss how the ES and Sk values affect the mean flows. Profiles of the inner-scaled streamwise mean velocity $\langle\overline{u}\rangle^+$ are presented in Fig. 4, where the effective wall-normal distance y_e:

$$y_e = \int_0^y \varphi dy, \tag{12}$$

proposed by Kuwata and Kawaguchi[18] is used as the distance from the rough wall. Notably, y_e becomes zero at the bottom of the deepest valley but returns to $y - h_m$ above the maximum roughness crest $y > h_p$[18]. For comparison, the DNS result for the smooth-wall case[36] is also included. As the present DNS considers the open-channel flows, the present smooth wall result deviates from the reference data for the full channel flow as it approaches the channel center. Nevertheless, the present DNS is in perfect agreement with the reference data near the wall region, thus indicating that the present grid resolution is sufficient to resolve the viscous sublayer near the wall.

The figure confirms that the profiles of $\langle\overline{u}\rangle^+$ for the rough-wall cases are shifted downward, which is due to an increase in the skin friction coefficient of the rough wall. The roughness function ΔU^+, evaluated as the difference in $\langle\overline{u}\rangle^+$ at $y_e^+ \simeq 100$ with the smooth-wall case results as in Kuwata and Kawaguchi[18], attains a maximum value of 7.3 ($Sk = +0.53$ and $ES = 0.6$), followed by 7.0 ($Sk = +0.53$ and $ES = 0.4$) and 5.3 ($Sk = -0.53$ and $ES = 0.6$). This indicates that the simulated flows are in the transitionally rough regime except the case with $Sk = +0.53$ and $ES = 0.6$, judging from the criterion of the fully rough regime[37] $\Delta U^+ \gtrsim 7 (k_s^+ > 70)$. For the case with $Sk = +0.53$ and $ES = 0.6$, where the flow is expected to be in the onset of the fully rough regime, the equivalent roughness height k_s^+ is estimated by the following relation[16]:

$$k_s^+ = exp\left[\kappa\left(8.5 - B + \Delta U^+\right)\right]. \tag{13}$$

In the above equation, $k_s^+ = 78$ when the von Kármán constant $\kappa = 0.41$ and the log-law intercept for a smooth $B = 5.2$ are used. Interestingly, this value reasonably agrees with the empirical correlation from the data for real rough surfaces[16] $k_s = 4.43h_{rms}(1+Sk)^{1.37}$ within 16%. This suggests that the generated surface yields hydraulic roughness effects comparable to real rough surfaces, despite the fact that the same surface geometry repeatedly appears in the streamwise and spanwise directions as mentioned in §III.

As for the influence of Sk, the figure confirms that ΔU^+ is larger for cases with the positive skewness value $Sk = +0.53$, which is consistent with the observations of previous studies[6,10,16,18,23]. Another observation from Fig. 4 is that ΔU^+ increases with the ES value: ΔU^+ substantially in-

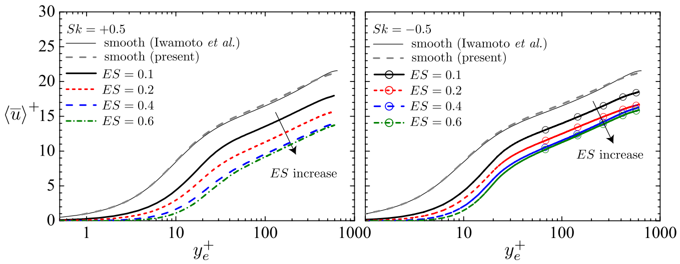

FIG. 4. Inner-scaled streamwise mean velocity profile. The DNS result for the smooth-wall case[36] is included.

creases as ES increases from 0.1 to 0.4, while this trend slows down when ES increases from 0.4 to 0.6.

The aforementioned is evident from Fig. 5, where ΔU^+ is plotted against the ES value. Also shown are the LES data for two-dimensional irregularly corrugated walls[5], the DNS data for three-dimensional sinusoidal roughness[9], and the experimental data for closely packed pyramids[8]. Note that the inner-scaled roughness height scales for the three-dimensional sinusoidal roughness[9] ($h^+_{rms} \simeq 5$) and the closely packed pyramids[8] ($h^+_{rms} \simeq 8.5$) are rather close to the values in the present study ($h^+_{rms} = 8.4$), whereas it is much larger in the two-dimensional irregularly corrugated wall[5] ($h^+_a = 19.5$) compared to the present study ($h^+_a = 6.7$). Figure 5 shows that ΔU^+ steeply increases with the ES value for the wavy surface regime[8] ($ES < 0.3$); however, this trend progressively weakens as the ES value further increases, which is consistent with the findings of previous studies[5,8]. The values of ΔU^+ in the present study are close to the values reported by Schultz and Flack[8] and Chan *et al.*[9], but deviate significantly from the results of Napoli *et al.*[5], in which the inner-scaled roughness height scales are significantly larger. This supports the findings by Chan *et al.*[9] that ΔU^+ depends on some measure of the viscous roughness height as well as the ES value. Another important observation from the figure is that the dependence of the ES value is generally similar irrespective of the Sk value; however, the influence of Sk on ΔU^+ is more pronounced for a surface with a large ES value: the difference in ΔU^+ is 20% when $ES = 0.1$ whereas the value is doubled when $ES = 0.6$.

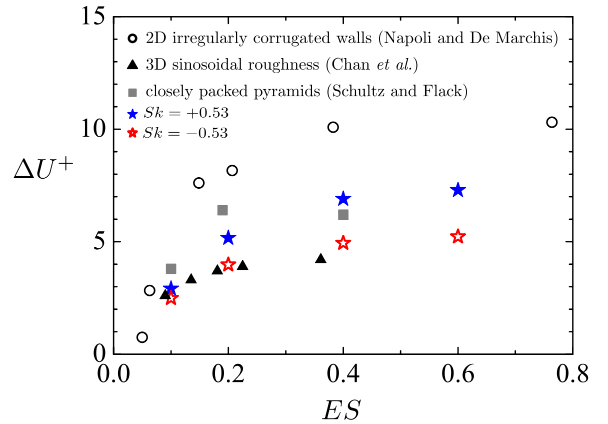

FIG. 5. Roughness function against the ES value. The LES data for two-dimensional irregularly corrugated walls[5], the DNS data for three-dimensional sinusoidal roughness[9], and the experimental data for closely packed pyramids[8] are plotted.

VI. MOMENTUM BUDGET

To better understand the physical mechanisms of the increase in friction drag, this section provides a discussion on momentum transfer with the help of the double-averaging theory. Applying the spatial- ($x-z$ plane) and Reynolds-averaging operators to the Navier–Stokes equation for incompressible flows, we can obtain the double-averaged momentum equation as follows:

$$\begin{aligned}\frac{\partial \langle \overline{u}_i \rangle}{\partial t} + \langle \overline{u}_j \rangle \frac{\partial \langle \overline{u}_i \rangle^f}{\partial x_j} = &-\frac{\varphi}{\rho}\frac{\partial \langle \overline{p} \rangle^f}{\partial x_i} + \frac{\partial}{\partial x_j}\left(\nu \frac{\partial \langle \overline{u}_i \rangle}{\partial x_j}\right) \\ &-\frac{\partial}{\partial x_j}\left(\underbrace{\langle \tilde{\overline{u}}_i \tilde{\overline{u}}_j \rangle}_{\mathscr{T}_{ij}} + \underbrace{\langle \overline{u'_i u'_j} \rangle}_{R_{ij}}\right) \\ &\underbrace{-\nu \frac{\partial \varphi}{\partial x_j}\frac{\partial \langle \overline{u}_i \rangle^f}{\partial x_j}}_{g_i} \\ &\underbrace{-\frac{1}{\rho S}\int_L \tilde{\overline{p}} n_i d\ell}_{f_{p_i}} \underbrace{-\frac{\nu}{S}\int_L \left(-n_k \frac{\partial \tilde{\overline{u}}_i}{\partial x_k}\right) d\ell}_{f_{v_i}},\end{aligned} \tag{14}$$

where L represents the obstacle perimeter within an averaging $x-z$ plane, ℓ represents the circumference length of solid obstacles, and n_k is its unit normal vector pointing outward from the fluid to solid phase. In addition to the plane-averaged Reynolds stress R_{ij}, a plane-dispersive covariance $\mathscr{T}_{ij}$ arises owing to the inhomogeneous nature of the mean flow in the $x-z$ plane, and is expressed as the product of the mean velocity dispersion $\tilde{\overline{u}}_i = \overline{u}_i - \langle \overline{u}_i \rangle^f$. The other terms representing the roughness effects are the inhomogeneous roughness density term g_i, the pressure drag term f_{p_i}, and the viscous drag force term f_{v_i}. The viscous and pressure drag force terms are expressed as the averaged pressure and viscous stress dispersions, respectively, over the obstacle perimeter at a certain plane. Hence, these terms represent the mean pressure and viscous forces offered by the roughness elements. As g_i originates from the volume-averaged viscous stress term, it represents the viscous effect arising from the distribution of the plane porosity φ, which exhibits a non-zero contribution only below the maximum roughness crest.

By integrating equation (14) over the wall-normal direction

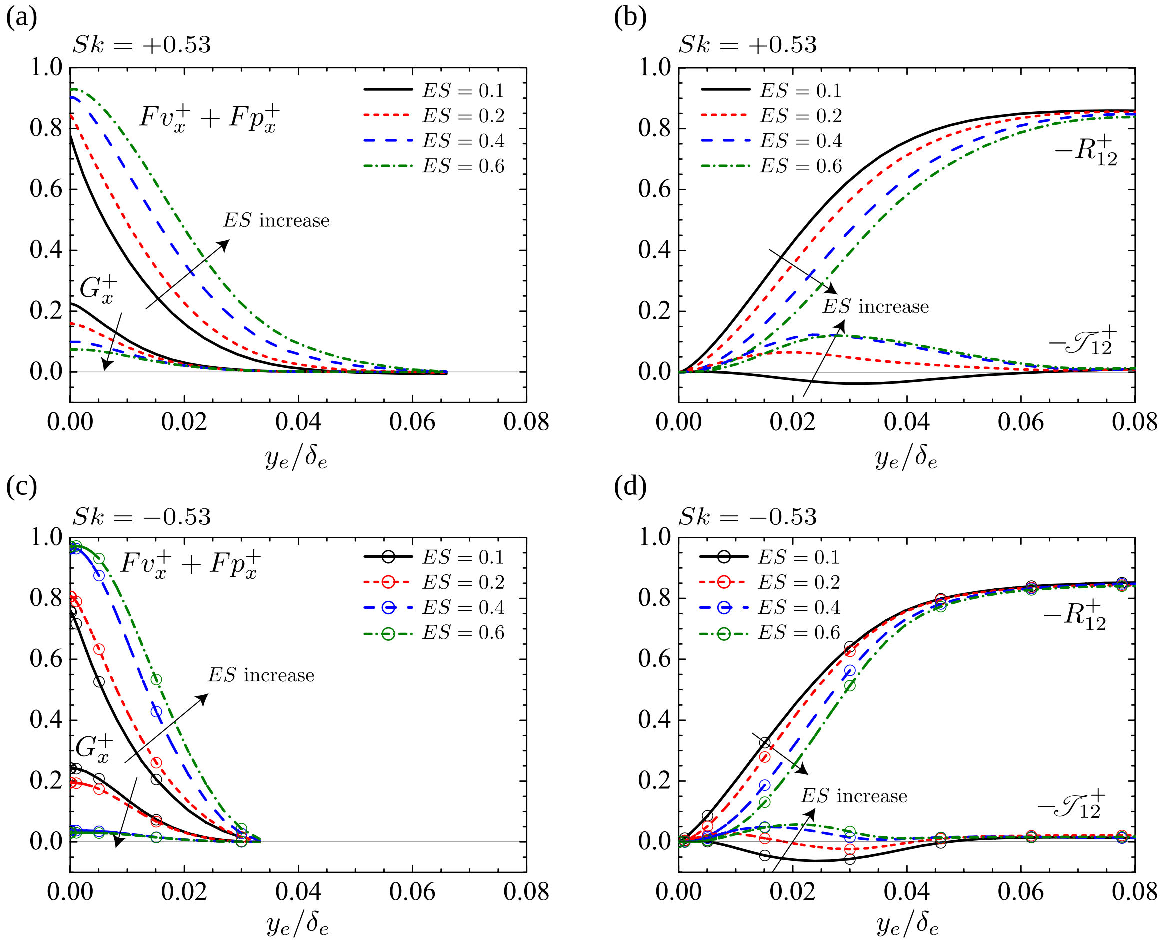

FIG. 6. Momentum budgets: (a) drag force contribution $Fv_x^+ + Fp_x^+$ and inhomogeneous roughness density contribution G_x^+ for surfaces with $Sk = +0.53$, (b) plane-averaged Reynolds stress $-R_{12}^+$ and plane-dispersive covariance $-\mathscr{T}_{12}$ for surfaces with $Sk = +0.53$, (c) $Fv_x^+ + Fp_x^+$ and G_x^+ for surfaces with $Sk = -0.53$, (d) $-R_{12}^+$ and $-\mathscr{T}_{12}$ for surfaces with $Sk = -0.53$.

from 0 to y and normalizing by u_τ, the shear stress balance for the present flow system in non-dimensional form can be derived after some manipulation[18]:

$$1 - \frac{y_e}{\delta_e} = \frac{\partial \langle \overline{u} \rangle^+}{\partial y^+} - R_{12}^+ - \mathscr{T}_{12}^+ + \underbrace{\int_y^{h_p} g_x^+ dy^+}_{G_x^+} + \underbrace{\int_y^{h_p} f_{v_x}^+ dy^+}_{Fv_x^+} + \underbrace{\int_y^{h_p} f_{p_x}^+ dy^+}_{Fp_x^+}, \tag{15}$$

where G_x^+, Fv_x^+, and Fp_x^+ denote the contributory terms of inhomogeneous roughness density, viscous drag, and pressure drag, respectively.

The contributions by the drag force $Fv_x^+ + Fp_x^+$, inhomogeneous roughness density G_x^+, plane-averaged Reynolds shear stress $-R_{12}^+$, and plane-dispersive covariance $-\mathscr{T}_{12}$ are shown in Fig. 6. Although the sum of the pressure and viscous drag forces is introduced here, each contribution is further detailed in §VII. In Fig. 6(a) for the peak-dominated surfaces with $Sk = +0.53$, the contribution by $Fv_x^+ + Fp_x^+$ is substantial below the roughness crest and monotonically increases with the ES value, whereas G_x^+ decreases with the ES value. In Fig. 6(b), as the ES value increases, $-\mathscr{T}_{12}^+$ increases while $-R_{12}^+$+ decreases. This indicates that $-\mathscr{T}_{12}^+$ and $-R_{12}^+$+ show a compensating effect, which is consistent with previous observations[18,23]. The reduction in $-R_{12}^+$ with the ES value was also found by MacDonald *et al.*[7] who explained that the turbulent near-wall cycle was pushed outward by the wall roughness for densely distributed roughness, which was characterized by the large ES value. For the valley-dominated surface with $Sk = -0.53$ in Fig. 6(c) and (d), although the maximum roughness crest measured by y_e is different from that for the case with $Sk = +0.53$, the general trend of the influence of the ES value on the momentum budget is qualitatively similar to that for the case with $Sk = +0.53$.

As can be seen in Fig. 6, the difference in the budget terms between the case with $Sk = +0.53$ and that with $Sk = -0.53$ appears to be responsible for the difference in the maximum roughness crest measured by y_e. To investigate the difference in detail, a comparison with the budget terms between the cases with $Sk = +0.53$ and $Sk = -0.53$ is presented in Fig.

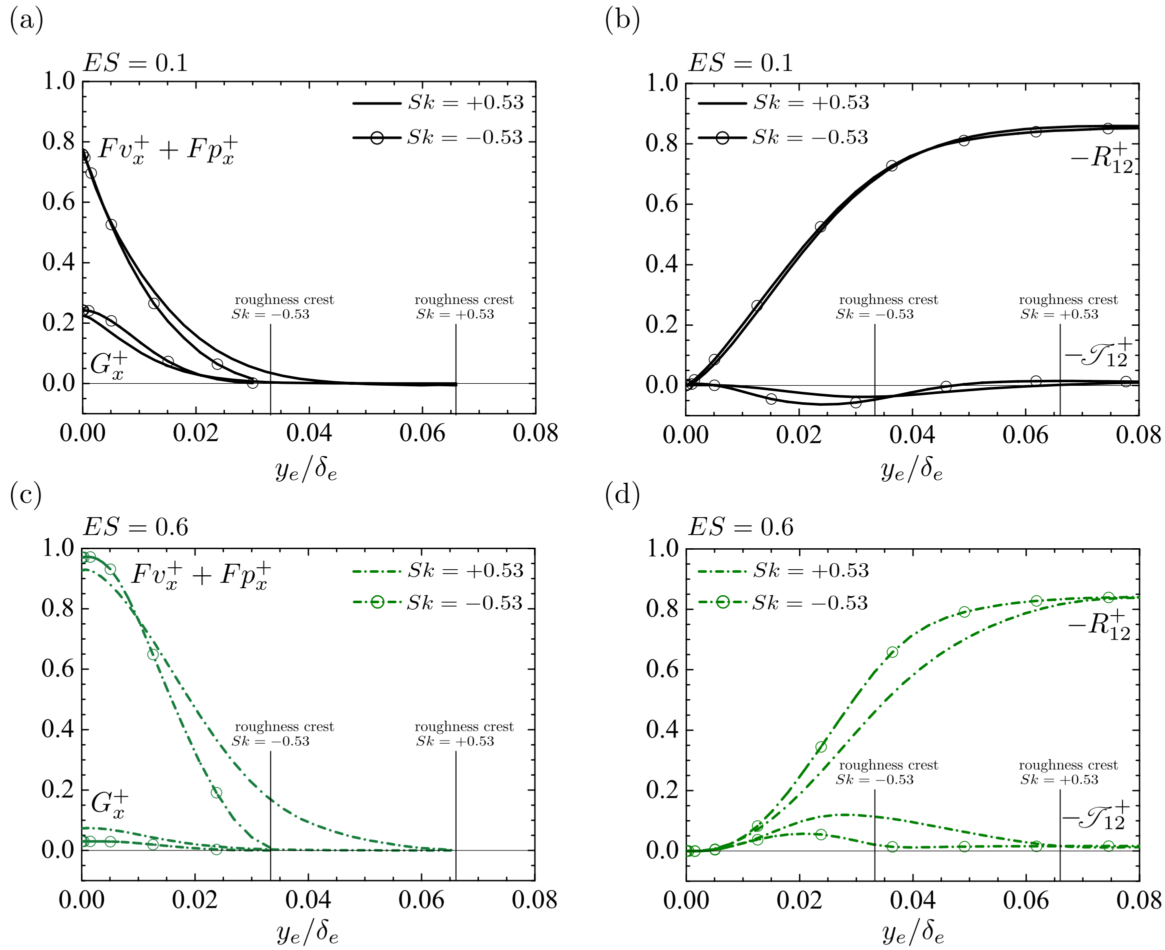

FIG. 7. Comparison of the momentum budgets for cases with $Sk = +0.53$ and $Sk = -0.53$: (a) $Fv_x^+ + Fp_x^+$ and G_x^+ for surfaces with $ES = 0.1$, (b) $-R_{12}^+$ and $-\mathscr{T}_{12}$ for surfaces with $ES = 0.1$, (c) $Fv_x^+ + Fp_x^+$ and G_x^+ for surfaces with $ES = 0.6$, (d) $-R_{12}^+$ and $-\mathscr{T}_{12}$ for surfaces with $ES = 0.6$.

7. It is evident from Fig. 7(a) and (c) that the drag force, $Fv_x^+ + Fp_x^+$, below the roughness crest ($0.03 < y_e < 0.07$) is significantly larger for the case with $ES = 0.6$ than that for the case with $ES = 0.1$, which enlarges the difference in the momentum budgets between the case with $Sk = +0.53$ and that with $Sk = -0.53$ ($ES = 0.6$) as shown in Fig. 7(c). As in $Fv_x^+ + Fp_x^+$, it is found from Fig. 7(b) and (d) that the difference in the second moments ($-R_{12}^+$ and $-\mathscr{T}_{12}^+$) is more pronounced for cases with $ES = 0.6$ below the roughness crest ($0.03 < y_e < 0.07$).

The physical interpretation of the influence of the ES values on the second moments can be provided by the spatial distribution of $-\tilde{\tilde{u}}\,\tilde{\tilde{v}}^+$ and $-\overline{u'v'}^+$ in the $x-z$ plane for the case with $Sk = +0.53$. Figures 8 and 10 depict the contour maps of $-\tilde{\tilde{u}}\,\tilde{\tilde{v}}^+$ and $-\overline{u'v'}^+$, respectively, at $y_e/\delta_e = 0.02$, where the effects of the ES values on R_{12}^+ and $\mathscr{T}_{12}^+$ are pronounced, as shown in Fig.6(b). Also shown are the contour lines to indicate the high-speed region and the backward flow region. The contour maps for $ES = 0.6$ in Figs. 10(b) and 8(b) are enlarged by a factor of 6 for a comparison with those for $ES = 0.1$. The dispersive shear stress of $-\tilde{\tilde{u}}\,\tilde{\tilde{v}}^+$ for the case with $ES = 0.1$ in Fig. 8 (a) is significant but the averaged value over the $x-z$ plane is considerably small ($-\left\langle\tilde{\tilde{u}}\,\tilde{\tilde{v}}\right\rangle^+ = -0.025$), thereby suggesting that there is almost no correlation between $\tilde{\tilde{u}}$ and $\tilde{\tilde{v}}$ for the case with $ES = 0.1$. In contrast, for the case with $ES = 0.6$ in Fig. 8 (b), although the magnitude of $-\tilde{\tilde{u}}\,\tilde{\tilde{v}}^+$ is not significant, $-\tilde{\tilde{u}}\,\tilde{\tilde{v}}$ tends to be positive for the high-speed and backward flow regions. This means that there is a strong negative correlation between $\tilde{\tilde{u}}$ and $\tilde{\tilde{v}}$ in the regions where the downwash flow of the high-speed fluid and upwash flow of the backward flow region frequently occur. The dominance of the negative dispersive shear stress for the case with $ES = 0.6$ can be statistically proven by Fig.9 where the joint probability density function of $\tilde{\tilde{u}}^+$ and $\tilde{\tilde{v}}^+$ is depicted. For the case with $ES = 0.6$ in Fig.9 (b), the occurrence of strong positive and negative $\tilde{\tilde{u}}^+$ is found to be less frequent than that for the case with $ES = 0.1$ in Fig.9 (a). However, it is apparent in Fig.9(b) that, for the case with $ES = 0.6$, there is a distinct negative correlation between $\tilde{\tilde{v}}^+$ and $\tilde{\tilde{u}}^+$, which produces the negative dispersion shear stress. This observation clearly explains the reason why $-\mathscr{T}_{12}^+$ increases with the ES values in Fig. 6(b).

The Reynolds shear stress $-\overline{u'v'}$ in Fig. 10 is generally positive, as in smooth-wall turbulence, but significantly reduced near the roughness elements. Interestingly, $-\overline{u'v'}$ is considerably larger for the case with $ES=0.1$ (Fig. 10(a)) than for the case with $ES=0.6$ (Fig. 10(b)) despite the fact that the skewness factor and roughness height scales are consistent. This difference can be reasonably explained from a snapshot of the instantaneous wall-normal vortex fluctuations shown in Fig. 11. In Fig. 11(a), quasi-streamwise vortices, which are similar to those in smooth-wall turbulence[38], develop for the case with $ES=0.1$ because of the sufficient scale separation between the roughness wavelength and the turbulent length scale. However, for the case with $ES=0.6$ in Fig. 11(b), as the roughness wavelength in the $x-$ and $z-$ directions is reduced by a factor of 6, the turbulent length scale is observed to be comparable to the roughness length scale. Consequently, the roughness elements effectively prevent the development of the quasi-streamwise vortices. A similar observation of the effects of the roughness on quasi-streamwise vortices was made by Kuwata and Kawaguchi[32]. Their budget term analysis suggested that the breakdown of quasi-streamwise vortice was a representation of additional energy dissipation due to a role of the drag force offered by the roughness elements. In other words, the turbulence generation tended to be attenuated with an increase in the drag force. This reasonably explains why $-\overline{u'v'}^{+}$ is smaller for the case with $ES=0.6$, in which the drag force contribution $Fv_x^+ + Fp_x^+$ is substantial within the rough wall, as shown in Fig. 6(a).

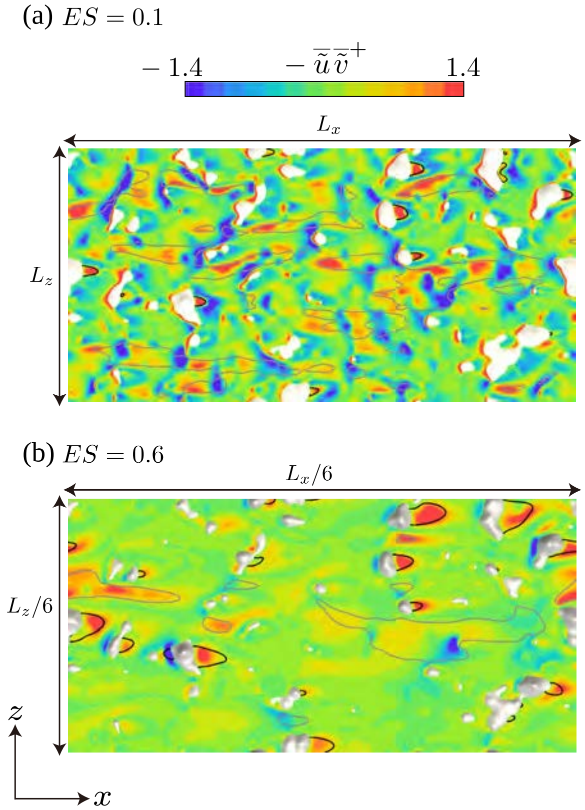

FIG. 8. Contour map of the dispersive shear stress $-\tilde{\bar{u}}\,\tilde{\bar{v}}^+$ in the $x-z$ plane at $y_e/\delta_e = 0.02$: (a) case with $ES=0.1$ and $Sk=+0.53$ and (b) case with $ES=0.6$ and $Sk=+0.53$. The regions enclosed by gray lines indicate the high-speed flow regions of $\overline{u}^+ > 0.8\overline{u}^+_{max}$, where $\overline{u}^+_{max}$ is the maximum velocity in the plane; those enclosed by black lines are the backward flow regions of $\overline{u}^+ < 0$.

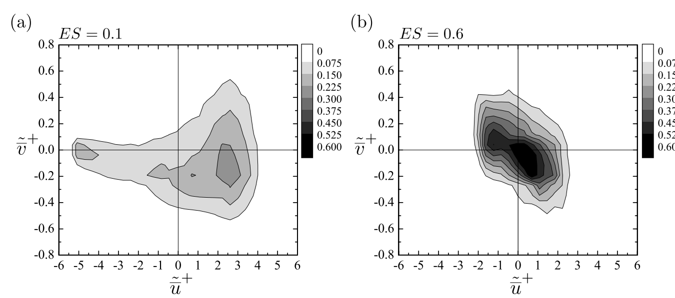

FIG. 9. Joint probability density function of the streamwise and wall-normal velocity dispersions: (a) case with $ES=0.1$ and $Sk=+0.53$ and (b) case with $ES=0.6$ and $Sk=+0.53$.

VII. CONTRIBUTION OF THE ROUGHNESS FUNCTION

Although the previous section concentrates on the influence of ES and Sk values on momentum transfer, it is still not clear how these momentum budget terms contribute to an increase in ΔU^+. Hence, in this section we quantify the effects on ΔU^+ starting from Eq. (15). The double-average momentum equation can be rewritten as follows:

$$\frac{\partial \varphi \langle \overline{u} \rangle^{f+}}{\partial y^+} = 1 - \frac{y_e}{\delta_e} + R^+_{12} + \mathscr{T}^+_{12} - G^+_x - Fv^+_x - Fp^+_x. \tag{16}$$

The left-hand side of Eq. (16) can be rewritten by using the definition of y_e in Eq. (12) as follows:

$$\frac{\partial \varphi \langle \overline{u} \rangle^{f+}}{\partial y^+} = \frac{\partial \varphi^2 \langle \overline{u} \rangle^{f+}}{\partial y^+_e} - \langle \overline{u} \rangle^{f+} \frac{\partial \varphi}{\partial y^+}. \tag{17}$$

By integrating Eq. (16) with Eq. (17) over the wall-normal direction from 0 to y^+_e, the mean velocity can be written in terms of the momentum budget terms as follows:

$$\begin{aligned} \varphi^2 \langle \overline{u} \rangle^{f+}(y^+_e) = {} & y^+_e \left(1 - \frac{1}{2}\frac{y^+_e}{Re_\tau}\right) + \int_0^{y^+_e} \left(R^+_{12} + \mathscr{T}^+_{12}\right) dy^+_e \\ & - \int_0^{y^+_e} \left(G^+_x - \langle \overline{u} \rangle^{f+} \frac{\partial \varphi}{\partial y^+}\right) dy^+_e \\ & - \int_0^{y^+_e} Fv^+_x dy^+_e - \int_0^{y^+_e} Fp^+_x dy^+_e. \end{aligned} \tag{18}$$

The corresponding equation for the smooth-wall case can be derived in a similar fashion as follows:

$$\langle \overline{u} \rangle^{f+}(y^+_e) = y^+_e \left(1 - \frac{1}{2}\frac{y^+_e}{Re_\tau}\right) + \int_0^{y^+_e} R^+_{12} dy^+_e. \tag{19}$$

Note that $y_e = y$ for the smooth-wall case because $\varphi = 1$. Subtracting the mean velocity for the rough-wall case in Eq. (18) from that for the smooth-wall case in Eq. (19) at $y^+_e = 100$, we can derive an expression for ΔU^+ in terms of several con-

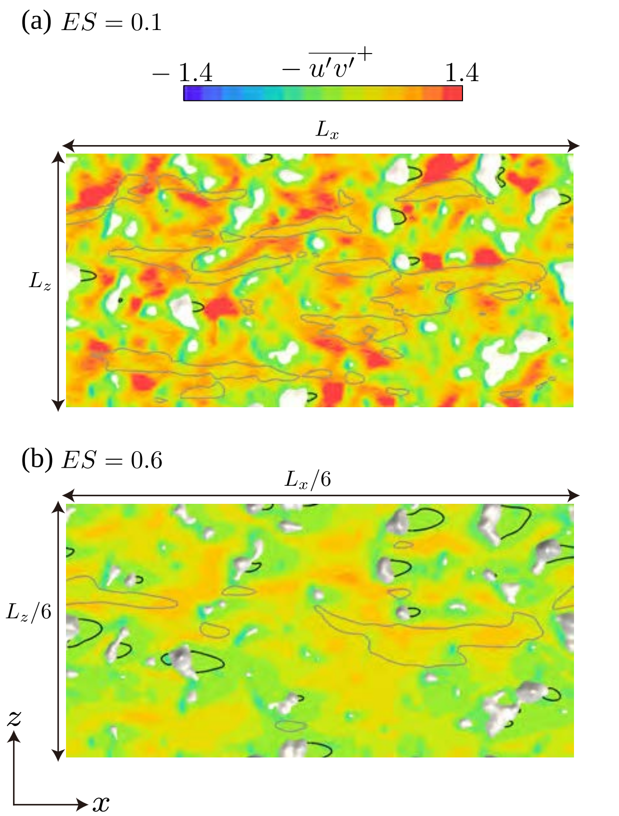

FIG. 10. Contour map of the Reynolds shear stress, $-\overline{u'v'}^+$, in the $x-z$ plane at $y_e/\delta_e = 0.02$: (a) case with $ES = 0.1$ and $Sk = +0.53$ and (b) case with $ES = 0.6$ and $Sk = +0.53$. The regions enclosed by gray lines indicate the high-speed flow regions of $\overline{u}^+ > 0.8\overline{u}^+_{max}$, where $\overline{u}^+_{max}$ is the maximum velocity in the plane; those enclosed by black lines are the backward flow regions of $\overline{u}^+ < 0$.

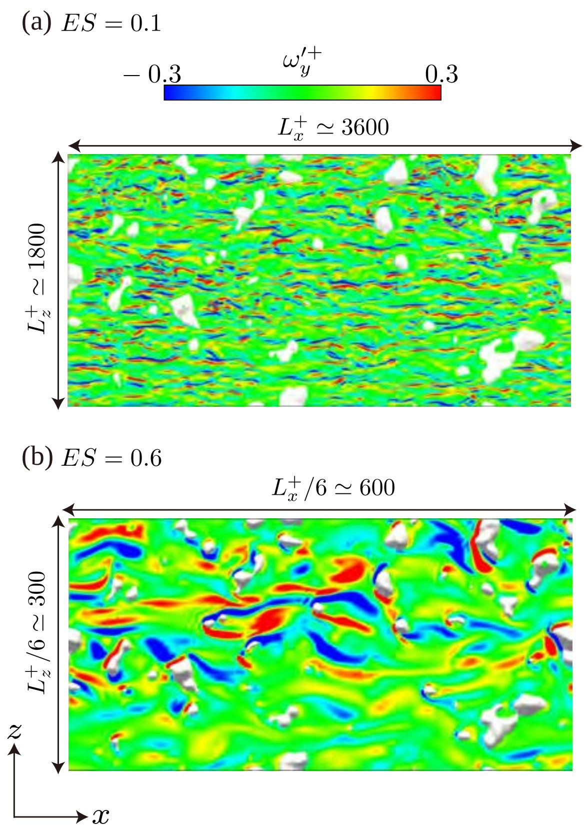

FIG. 11. Snapshot of the wall-normal vorticity fluctuations in the $x-z$ plane at $y_e/\delta_e = 0.02$: (a) case with $ES = 0.1$ and $Sk = +0.53$ and (b) case with $ES = 0.6$ and $Sk = +0.53$.

tributors, as follows:

$$\begin{aligned}
\Delta U^+ &= \Delta U^+_{sm} + \Delta U^+_{dv} + \Delta U^+_{dp} + \Delta U^+_{ir}, \\
\Delta U^+_{sm} &= \int_0^{100} R^+_{12} dy^+_e \Big|_{smooth} - \int_0^{100} \left(R^+_{12} + \mathscr{T}^+_{12}\right) dy^+_e \Big|_{rough}, \\
\Delta U^+_{dv} &= \int_0^{h^+_{pe}} F v^+_x dy^+_e \Big|_{rough}, \\
\Delta U^+_{dp} &= \int_0^{h^+_{pe}} F p^+_x dy^+_e \Big|_{rough}, \\
\Delta U^+_{ir} &= \int_0^{h^+_{pe}} \left(G^+_x - \langle u \rangle^{f+} \frac{\partial \varphi}{\partial y^+}\right) dy^+_e \Big|_{rough},
\end{aligned} \tag{20}$$

where h_{pe} is the maximum roughness crest evaluated by y_e, and the contributors ΔU^+_{sm}, ΔU^+_{dv}, ΔU^+_{dp}, and ΔU^+_{ir} represent the effects of the second moment, viscous drag, pressure drag, and inhomogeneous roughness terms, respectively. It is to be noted that MacDonald *et al.*[7] as well as Jelly and Busse[23] derived similar expressions for ΔU; however, they did not separately consider the contributions of ΔU^+_{dv}, ΔU^+_{dp}, and ΔU^+_{ir}, which have a dominant effect below the roughness crest. The contributors in Eq.(20) are shown in Fig. 12. The figure confirms that ΔU^+ is dominated by the pressure and viscous drag effects (ΔU^+_{dv} and ΔU^+_{dp}), whereas the second moment ΔU^+_{sm} exhibits a negative contribution. The viscous drag ΔU^+_{dv} dominates ΔU^+ when $ES = 0.1$ but does not increase with the ES value; however, ΔU^+_{dp} dramatically increases with the ES value, which supports the findings by Napoli *et al.*[5] as well as Leonardi and Castro[13], who showed that the contribution of the pressure drag to the friction drag increased with an increasing ES value. A comparison between the results for the case with $Sk = +0.53$ and that with $Sk = -0.53$ suggests that ΔU^+_{dp} is consistently larger for the peak-dominated surface with $Sk = +0.53$ and that this is the dominant mechanism leading to the larger ΔU^+ for the peak-dominated surface. The negative contribution of ΔU^+_{sm} is more significant as the ES value increases, i.e., the friction drag associated with $-(R^+_{12} + \mathscr{T}^+_{12})$ is less significant than that for the smooth-wall case and decreases with the ES value. This is principally due to the significant reduction in $-R^+_{12}$ with the ES value, as observed in Fig. 6(b) and (d). Another notable observation from Fig. 12 is that the negative contribution by ΔU^+_{sm} for cases with $ES \geq 0.4$ partly cancels the positive contributions by ΔU^+_{dv} and ΔU^+_{pd}, which explains why ΔU^+ does not significantly increase with the ES value for the roughness regime ($ES \geq 0.4$) as observed in Fig. 5.

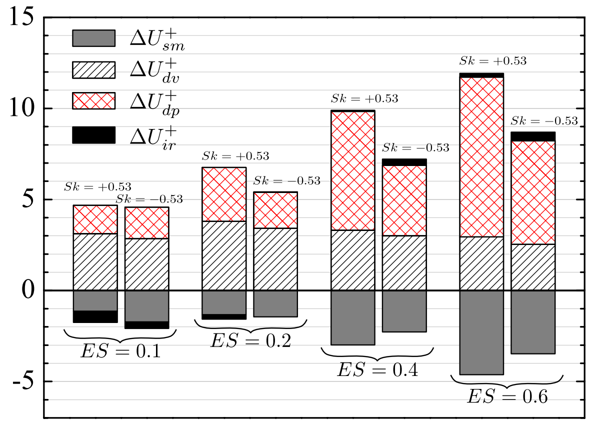

FIG. 12. Contribution of the roughness function. The contributory terms: ΔU^+_{sm} is the second moment, ΔU^+_{dv} is the viscous drag, ΔU^+_{dp} is the pressure drag, and ΔU^+_{ir} represents inhomogeneous roughness, which are expressed as Eq. (20).

VIII. DRAG FORCE

In this section, we describe an attempt to obtain a physical understanding of the drag force effects expressed as ΔU^+_{dv} and ΔU^+_{dp}. The viscous drag contributor, which is expressed as the double integral of $f^+_{v_x}$, can be transformed by partial integration as follows:

$$\begin{aligned}\Delta U^+_{dv} &= \int_0^{h^+_{pe}} \left(\int_{y^+}^{h^+_p} f^+_{v_x} dy^+ \right) dy^+_e \\ &= \int_0^{h^+_p} \frac{dy^+_e}{dy^+} \left(\int_{y^+}^{h^+_p} f^+_{v_x} dy^+ \right) dy^+ \\ &= \left[y^+_e \left(\int_{y^+}^{h^+_p} f^+_{v_x} dy^+ \right) \right]_0^{h^+_p} \\ &\quad - \int_0^{h^+_p} y^+_e \frac{d}{dy^+} \left(\int_{y^+}^{h^+_p} f^+_{v_x} dy^+ \right) dy^+, \end{aligned} \tag{21}$$

As $y^+_e = 0$ when $y^+ = 0$, the definite integral in the first term on the right-hand side of Eq. (21) goes to zero as follows:

$$\left[y^+_e \left(\int_{y^+}^{h^+_p} f^+_{v_x} dy^+ \right) \right]_0^{h^+_p} = 0. \tag{22}$$

In addition, the differentiation of the definite integral in the second term on the right-hand side of Eq. (21) can be written as

$$\frac{d}{dy^+} \left(\int_{y^+}^{h^+_p} f^+_{v_x} dy^+ \right) = -f^+_{v_x}. \tag{23}$$

Substituting Eqs.(22) and (23) into Eq. (21), the contribution by the viscous drag force can be simply expressed as the weighted integral of $f^+_{p_x}$, as follows:

$$\Delta U^+_{dv} = \int_0^{h^+_p} y^+_e f^+_{v_x} dy^+. \tag{24}$$

The contribution by the pressure drag can be expressed in a similar fashion as follows:

$$\Delta U^+_{dp} = \int_0^{h^+_p} y^+_e f^+_{p_x} dy^+. \tag{25}$$

The interesting implication from Eqs.(24) and (25) is that ΔU^+ is not solely affected by the magnitude of $f^+_{p_x}$ or $f^+_{v_x}$ itself; rather, the product of the effective distance y_e and the drag force is the key factor. First, the dominant mechanism of the increase in ΔU^+, namely the pressure drag effects, is shown against y/h and $y^* = (y - h_m)/h_{rms}$ in Fig. 13. In Fig. 13 (a) and (b), as the ES value increases, $f^+_{p_x}$ progressively increases above the mean location of the surface ($y^* > 0$) but decreases near the bottom ($-2 < y^* < -1$). The primary reason for the increase in $f^+_{p_x}$ is an increase in the wetted area of the rough surface with the ES value: the wetted area is proportional to the ES value for the surfaces considered in this study, and thus it increases by a factor of 6 as ES increases from 0.1 to 0.6. It is worth noting that the effective distance y_e increases with y/δ as shown in Fig. 13(a) and (b). Hence, $f^+_{p_x}$ near the bottom wall plays a less important role in $y^+_e f^+_{p_x}$ but is more influential as it moves toward the roughness crest. This can be clearly confirmed from Fig. 13 (c) and (d): the decrease in $f^+_{p_x}$ with the ES value below the mean location of the surface ($y^* < 0$) is less visible for $y^+_e f^+_{p_x}$, while the increase in $f^+_{p_x}$ with the ES value near the roughness crest is enlarged. Consequently, it can be concluded that ΔU^+ increases with the ES value, owing to the increase in $f^+_{p_x}$ above the mean location of the surface.

A comparison of $f^+_{p_x}$ for the case with $Sk = +0.53$ (Fig. 13(a)) against the case with $Sk = -0.53$ (Fig. 13(b)) confirms that the location where $f^+_{p_x}$ reaches the maximum peak value is almost the same when scaled by y^* as $0 < y^* < 1$, while the maximum peak value of $f^+_{p_x}$ is found to be larger for the valley-dominated surface ($Sk = -0.53$) when the ES value is the same. However, y^+_e against y/δ is considerably larger for cases with $Sk = +0.53$; thus, the difference in the maximum peak value of $f^+_{p_x}$ becomes considerably smaller for $y^+_e f^+_{p_x}$, as shown in Fig. 13(c) and (d). As a result, the integral of $y^+_p f^+_{p_x}$ expressed as Eq. (25) becomes larger for the surface with $Sk = +0.53$. This is the reason why the contribution of the pressure drag ΔU^+ is larger for the surface with $Sk = +0.53$.

The viscous drag $f^+_{v_x}$ and the weighted viscous drag $y^+_e f^+_{v_x}$ are also presented in Fig. 14. Figure 14 (a) and (b) confirms that, in contrast with the pressure drag, the maximum peak of $f^+_{v_x}$ generally decreases with the ES value despite the increase in the wetted area of the rough surface. In the region of $-2 < y^* < 1$, $f^+_{v_x}$ rapidly decreases with the ES value and eventually exhibits a negative value for the cases with $ES = 0.4$ and 0.6. This trend is consistent irrespective of the Sk value. However, as the effective distance y^+_e is not significant in those regions, the significant reduction of $f^+_{v_x}$ with the ES value is less influential for $y^+_e f^+_{v_x}$, which explains why the contribution of the roughness ΔU_{dp} is not significantly affected by the ES value, as shown in Fig. 12.

Finally, we focus on the influence of ES values on the mean flow structure, which is closely related to the drag force terms

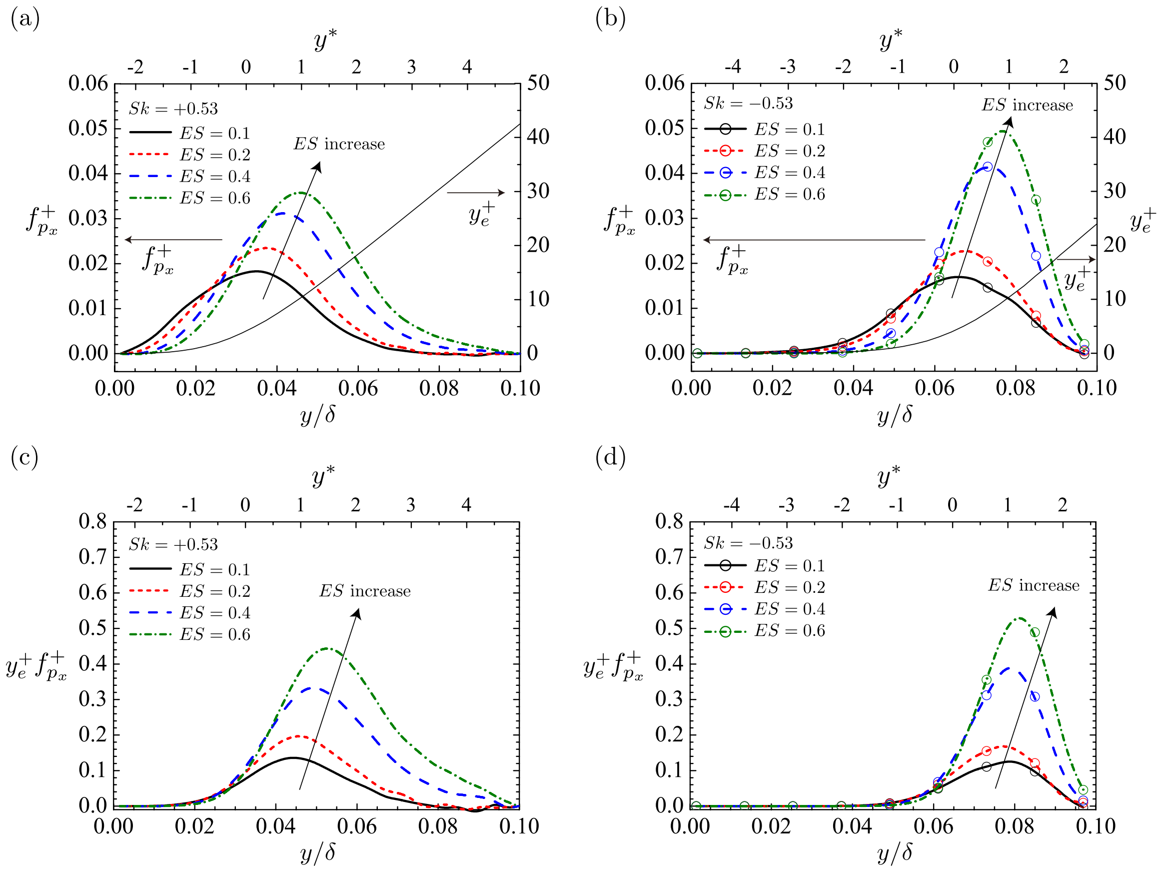

FIG. 13. Profiles of the pressure drag against y/h and $y^* = (y - h_m)/h_{rms}$: (a) pressure drag $f^+_{p_x}$ for cases with $Sk = +0.53$, (b) $f^+_{p_x}$ for cases with $Sk = -0.53$, (c) weighted pressure drag $y^+_e f^+_{p_x}$ for cases with $Sk = +0.53$, and (d) $y^+_e f^+_{p_x}$ for cases with $Sk = -0.53$. Thin solid lines in (a) and (b) indicate the profiles of y^+_e.

$f^+_{v_x}$ and $f^+_{p_x}$. The PDF of $\overline{u}^+$ below the roughness crest is shown for the case with $Sk = +0.53$ in Fig. 15. As aforementioned, the influence of the ES value on the drag force terms is similar irrespective of the Sk values, and only the results for the case with $Sk = +0.53$ are shown here (we have confirmed that the same conclusion can be drawn for the case with $Sk = -0.53$). In Fig. 15(a) and (b), the most notable difference between the results for the cases with $ES = 0.1$ and $ES = 0.6$ is the probability density of the backward flow near the location of the mean surface $y^* = -0.12$: although a weak backward flow with $-1 < \overline{u}^+ < 0$ occurs in both cases, the PDF of $-1 < \overline{u}^+ < 0$ significantly increases for the case with $ES = 0.6$, indicating an increase in the weak backward flow region. For the case with $ES = 0.6$, the PDFs at $y^* = -0.12$ and 0.53 exhibit peaks around $\overline{u}^+ \simeq 0$, indicating that the flow field is dominated by the dead water region where the mean positive or negative flow is sufficiently weak to interact with outer flows. In the dead water region, the wall-shear stress is very minimal and sometimes shows a negative value; thus, $f^+_{v_x}$ for the case with $ES = 0.6$ exhibits a smaller value than that for the case with $ES = 0.1$ near the location of the mean surface, as observed in Fig. 14(a). Further, in this region the mean pressure dispersion is considerably small, which may explain the reason why $f^+_{p_x}$ below the location of the mean surface decreases with the ES value in Fig. 13(a).

The increase in the dead flow regions near the location of the mean surface can be confirmed by a contour map of the streamwise mean velocity at $y^* = -0.12$ in Fig. 16 together with contour lines of $\overline{u} = 0$. It is immediately observed that the weak backward flow regions ($-2 < \overline{u}^+ < 0$) associated with the recirculating bubbles behind the roughness elements are merged and significantly extended for the case with $ES = 0.6$ in Fig. 16(b), while the backward flow regions for the case with $ES = 0.1$ in Fig. 16(a) are limited to the region immediately behind the roughness elements. This is principally due to insufficient scale separation between the roughness wavelength and the turbulent length scale for the dense roughness ($ES = 0.6$), as shown in Fig. 11(b). In this situation, the turbulent vortices do not penetrate the dead water region, and the stable weak vortices within the roughness, which are driven by the skimming flow above the roughness crest, are not disrupted by the turbulent vortices. Therefore, the mean flow structure is analogous to that seen in $d-$ type roughness[14,39,40].

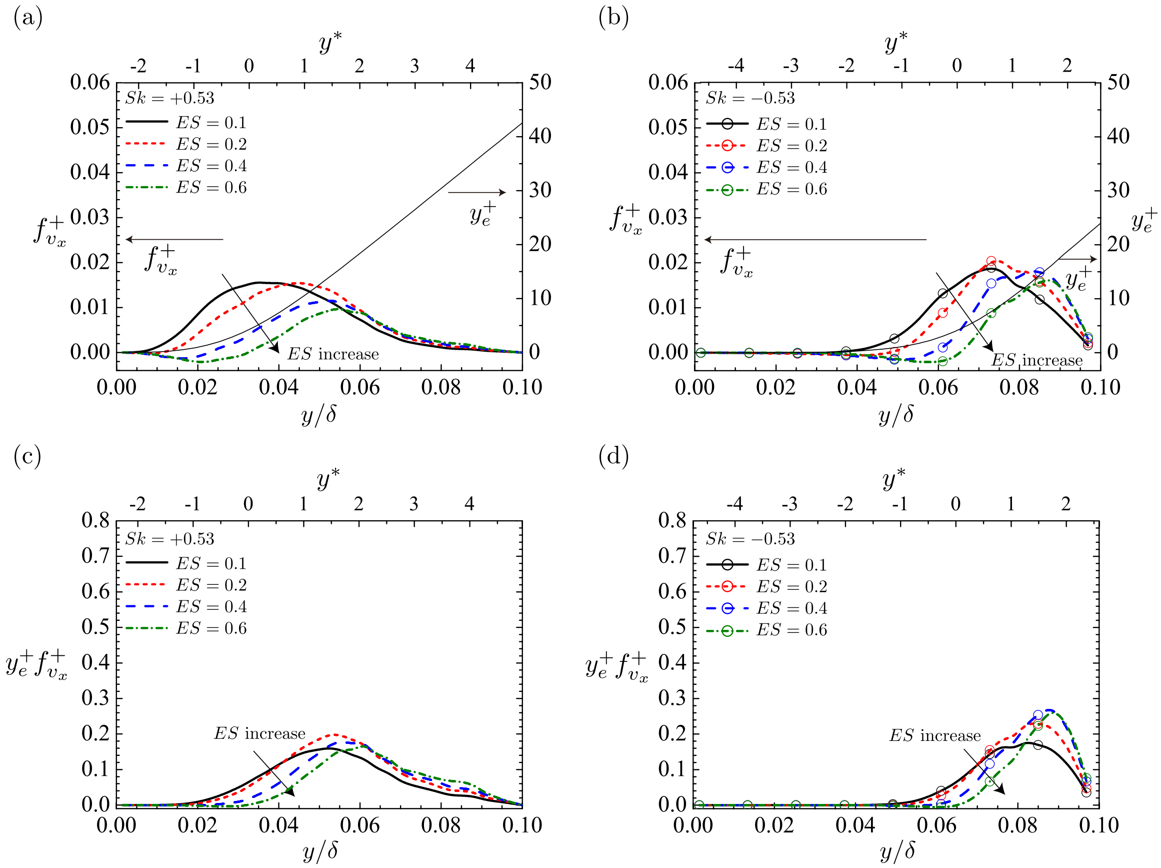

FIG. 14. Profiles of the viscous drag against y/h and $y^* = (y - h_m)/h_{rms}$: (a) viscous drag $f^+_{v_x}$ for cases with $Sk = +0.53$, (b) $f^+_{v_x}$ for cases with $Sk = -0.53$, (c) weighted viscous drag $y^+_e f^+_{v_x}$ for cases with $Sk = +0.53$, and (d) $y^+_e f^+_{v_x}$ for cases with $Sk = -0.53$. Thin solid lines in (a) and (b) indicate the profiles of y^+_e.

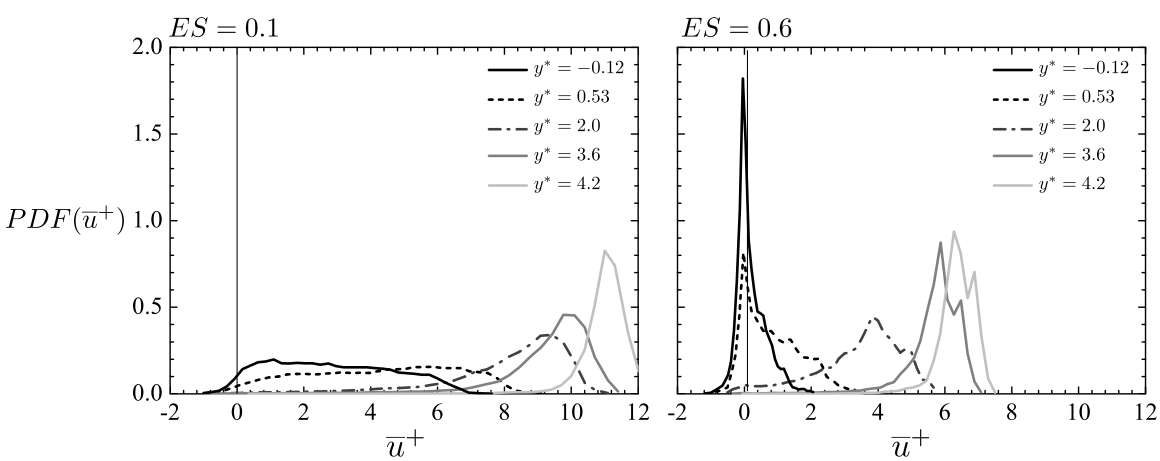

FIG. 15. PDF of the streamwise mean velocity, $\overline{u}^+$, in the $x-z$ plane at different y^* locations for cases with $Sk = +0.53$.

IX. CONCLUSIONS

The influence of two important geometrical parameters for rough surfaces, namely, the effective slope ES and skewness factor Sk, on rough wall turbulence was analyzed by DNSs of turbulence over systematically varied three-dimensional irregular rough surfaces. We numerically generated the rough surfaces in which the ES and Sk values were systematically varied in the range of $Sk = \pm 0.53$ and $0.1 \le ES \le 0.6$, while roughness height scales remained fixed.

We confirmed that the roughness function ΔU^+ is larger for a peak-dominated surface with $Sk = +0.53$ than that for a

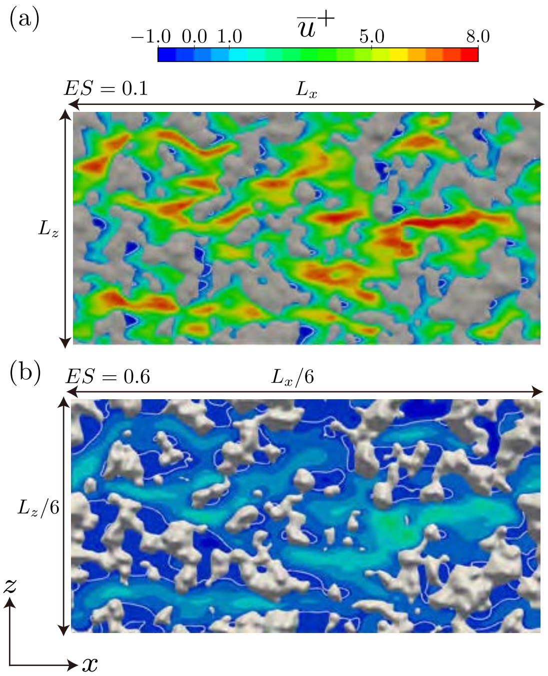

FIG. 16. Contour map of the streamwise mean velocity $\overline{u}^+$ in the $x-z$ plane at $y_e/\delta_e = 0.02$ for cases with $Sk = +0.53$: (a) for case with $ES = 0.1$ and (b) for case with $ES = 0.6$. The regions enclosed by white lines are the backward flow regions of $\overline{u}^+ < 0$.

valley-dominated surface with $Sk = -0.53$. The dependence of Sk on ΔU^+ increases as the ES value increases. As for the influence of ES, it was found that ΔU^+ steeply increases when $0.1 \leq ES \leq 0.4$ whereas the increase slows down when $ES \geq 0.4$.

The physical mechanism behind the increase in ΔU^+ was discussed by analyzing the spatial- and Reynolds-averaged momentum equation. For a surface with $ES \leq 0.2$, the viscous drag dominantly contributes to ΔU^+, whereas the contribution by the pressure drag progressively increases with the ES value and becomes dominant when $ES \geq 0.4$. Meanwhile, when $ES \geq 0.4$, as there is no sufficient scale separation between the roughness wavelength and the turbulent length scale, the wall roughness prevents the formation of quasi-streamwise elongated vortices that suppress the turbulent near-wall cycles, thereby decreasing the Reynolds shear stress. This acts as a negative contribution to ΔU^+, and the two aforementioned competing effects weaken the dependence of the ES value on ΔU^+ when $ES \geq 0.4$. As for the influence of the Sk value, the pressure drag is consistently larger for the surface with $Sk = +0.53$; this is the dominant mechanism leading to the larger ΔU^+ for the surface with $Sk = +0.53$.

The drag force effects, which have a dominant impact on the increase in ΔU^+, were further analyzed. The contribution of ΔU^+ by the drag force was found to be the integral of the weighted drag force, which is expressed as the product of the drag force and effective distance from within the rough walls. Because the effective distance increases as it approaches the roughness crest, the drag force near the roughness crest provides a larger contribution to the increase in ΔU^+. The effective distance, which depends on the geometry of the rough surfaces, is generally larger for a surface with $Sk = +0.53$, thus leading to the increase in the drag force contribution to ΔU^+ for the surface with $Sk = +0.53$. This is the main reason why peak-dominated surfaces with a positive Sk yield larger ΔU^+.

The present strategy for varying surface characteristics was found to be meaningful in investigating the isolated effects of the effective slope ES and skewness factor Sk. However, the present study only considers a single relatively low friction Reynolds number of 600, owing to limitations in computational resources; thus, the simulated flows are generally in the transitionally rough regime. Further analysis in the fully rough regime will be required for full appreciation of the effects. This will be accomplished through experiments or minimal flow simulations as in Macdonald *et al.*[41].

ACKNOWLEDGMENTS

The authors express their gratitude to their colleagues, Dr. K. Suga and Dr. M. Kaneda, for their support. A part of this study was financially supported by JSPS Japan (No.17K1459). The numerical calculations were carried out on the TSUBAME3.0 supercomputer at Tokyo Institute of Technology in research projects (ID: hp180052).

DATA AVAILABILITY

The data that support the findings of this study are available from the corresponding author upon reasonable request.

[1]D. Bettermann, *Contribution a l'etude de la couche limite turbulente le long de plaques rugueses*, CNRS/LA-65/6 (CNRS, 1965).
[2]F. Dvorak, "Calculation of turbulent boundary layers on rough surfaces in pressure gradient." AIAA journal **7**, 1752–1759 (1969).
[3]R. Dirling, JR, "A method for computing roughwall heat transfer rates on reentry nosetips," in *8th Thermophysics Conference* (1973) p. 763.
[4]A. Sigal and J. Danberg, "New correlation of roughness density effect on the turbulent boundary layer," AIAA journal **28**, 554–556 (1990).
[5]E. Napoli, V. Armenio, and M. De Marchis, "The effect of the slope of irregularly distributed roughness elements on turbulent wall-bounded flows," J. Fluid Mech. **613**, 385–394 (2008).
[6]M. Thakkar, A. Busse, and N. D. Sandham, "Surface correlations of hydrodynamic drag for transitionally rough engineering surfaces," J. Turb. **18**, 138–169 (2017).
[7]M. MacDonald, L. Chan, D. Chung, N. Hutchins, and A. Ooi, "Turbulent flow over transitionally rough surfaces with varying roughness densities," J. Fluid Mech. **804**, 130–161 (2016).
[8]M. P. Schultz and K. A. Flack, "Turbulent boundary layers on a systematically varied rough wall," Phys. Fluids **21**, 015104 (2009).
[9]L. Chan, M. MacDonald, D. Chung, N. Hutchins, and A. Ooi, "A systematic investigation of roughness height and wavelength in turbulent pipe flow in the transitionally rough regime," J. Fluid Mech. **771**, 743–777 (2015).
[10]P. Forooghi, A. Stroh, F. Magagnato, S. Jakirlić, and B. Frohnapfel, "Toward a universal roughness correlation," J. Fluids Engng. **139**, 121201 (2017).
[11]M. De Marchis, "Large eddy simulations of roughened channel flows: Estimation of the energy losses using the slope of the roughness," Comput. Fluids **140**, 148–157 (2016).
[12]J. Yuan and M. A. Jouybari, "Topographical effects of roughness on turbulence statistics in roughness sublayer," Phys. Rev. Fluids **3**, 114603 (2018).

[13]S. Leonardi and I. Castro, "Channel flow over large cube roughness: a direct numerical simulation study," J. Fluid Mech. **651**, 519–539 (2010).
[14]A. Perry, W. Schofield, and P. Joubert, "Rough wall turbulent boundary layers," J. Fluid Mech. **37**, 383–413 (1969).
[15]A. Musker, "Universal roughness functions for naturally-occurring surfaces," Trans. Canadian Soc. Mech. Engng. **6**, 1–6 (1980).
[16]K. A. Flack and M. P. Schultz, "Review of hydraulic roughness scales in the fully rough regime," J. Fluids Engng. **132**, 041203 (2010).
[17]K. A. Flack, M. P. Schultz, J. M. Barros, and Y. C. Kim, "Skin-friction behavior in the transitionally-rough regime," Int. J. Heat Fluid Flow **61**, 21–30 (2016).
[18]Y. Kuwata and Y. Kawaguchi, "Direct numerical simulation of turbulence over systematically varied irregular rough surfaces," J. Fluid Mech. **862**, 781–815 (2019).
[19]J. Yuan and U. Piomelli, "Roughness effects on the reynolds stress budgets in near-wall turbulence," J. Fluid Mech. **760** (2014).
[20]A. Busse, M. Thakkar, and N. Sandham, "Reynolds-number dependence of the near-wall flow over irregular rough surfaces," J Fluid Mech. **810**, 196–224 (2017).
[21]K. Flack, M. Schultz, and R. Volino, "The effect of a systematic change in surface roughness skewness on turbulence and drag," Int. J. Heat Fluid Flow **85**, 108669 (2020).
[22]K. Flack, M. Schultz, and J. Barros, "Skin friction measurements of systematically-varied roughness: Probing the role of roughness amplitude and skewness," Flow, Turb. Combust. **104**, 317–329 (2020).
[23]T. Jelly and A. Busse, "Reynolds and dispersive shear stress contributions above highly skewed roughness," J. Fluid Mech. **852**, 710–724 (2018).
[24]J. Barros, M. Schultz, and K. Flack, "Measurements of skin-friction of systematically generated surface roughness," Int. J. Heat Fluid Flow **72**, 1–7 (2018).
[25]M. De Marchis, B. Milici, and E. Napoli, "Numerical observations of turbulence structure modification in channel flow over 2D and 3D rough walls," Int. J. Heat and Fluid Flow **56**, 108–123 (2015).
[26]P. Forooghi, A. Stroh, P. Schlatter, and B. Frohnapfel, "Direct numerical simulation of flow over dissimilar, randomly distributed roughness elements: A systematic study on the effect of surface morphology on turbulence," Phys. Rev. Fluids **3**, 044605 (2018).
[27]O. Coceal, T. Thomas, I. Castro, and S. Belcher, "Mean flow and turbulence statistics over groups of urban-like cubical obstacles," Boundary Layer Meteorol. **121**, 491–519 (2006).
[28]Y. Kuwata and Y. Kawaguchi, "Statistical discussions on skin frictional drag of turbulence over randomly distributed semi-spheres," Int. J. Adv. Engng. Sci. Appl. Mat. , 1–10 (2018).
[29]Y. Kuwata, T. Sugiyama, and Y. Kawaguchi, "On the scaling of turbulence over an irregular rough surface in a transitionally rough regime," J. Therm.l Sci. Tech. **15**, 0015 (2020).
[30]K. Suga, Y. Kuwata, K. Takashima, and R. Chikasue, "A D3Q27 multiple-relaxation-time lattice Boltzmann method for turbulent flows," Comput. Math. Appl. **69**, 518–529 (2015).
[31]Y. Kuwata and K. Suga, "Lattice boltzmann direct numerical simulation of interface turbulence over porous and rough walls," Int. J. Heat Fluid Flow **61**, 145–157 (2016).
[32]Y. Kuwata and Y. Kawaguchi, "Direct numerical simulation of turbulence over resolved and modelled rough walls with irregularly distributed roughness," Int. J. Heat Fluid Flow. submitted (2018).
[33]Y. Kuwata and K. Suga, "Imbalance-correction grid-refinement method for lattice Boltzmann flow simulations," J. Comput. Phys. **311**, 348–362 (2016).
[34]C. Pan, L.-S. Luo, and C. T. Miller, "An evaluation of lattice boltzmann schemes for porous medium flow simulation," Comput. Fluids **35**, 898–909 (2006).
[35]Y. Kuwata and K. Suga, "Transport mechanism of interface turbulence over porous and rough walls," Flow, Turb. Combust. **97**, 1071–1093 (2016).
[36]K. Iwamoto, Y. Suzuki, and N. Kasagi, "Database of fully developed channel flow-thtlab internal report no," ILR-0201, Rapport technique, THT-LAB, Dept. of Mech. Engng., The Univ. of Tokyo (2002).
[37]J. Nikuradse, "Laws of flow in rough pipes," in *VDI Forschungsheft* (Citeseer, 1933).
[38]J. Kim, P. Moin, and R. Moser, "Turbulence statistics in fully developed channel flow at low Reynolds number," J. Fluid Mech. **177**, 133–166 (1987).
[39]T. Oke, "Street design and urban canopy layer climate," Energy and buildings **11**, 103–113 (1988).
[40]J. Jiménez, "Turbulent flows over rough walls," Annu. Rev. Fluid Mech. **36**, 173–196 (2004).
[41]M. MacDonald, D. Chung, N. Hutchins, L. Chan, A. Ooi, and R. García-Mayoral, "The minimal-span channel for rough-wall turbulent flows," J. Fluid Mech. **816**, 5–42 (2017).